A unique polymer-inorganic cathode-electrolyte-interphase (CEI) boosts high-performance $Na_3V_2(PO_4)_2F_3$ batteries in ether electrolytes

Bingsheng Qin [a,b,c], Maider Zarrabeitia [a,b], Alexander Hoefling [a,b], Zenonas Jusys [d], Xu Liu [a,b], Jens Tübke [a,b], R. Jurgen Behm [a,d], Guanglei Cui [c,*], Alberto Varzi [a,b,**], Stefano Passerini [a,b,***]

[a] *Helmholtz Institute Ulm (HIU), Helmholtzstraße 11, D-89081, Ulm, Germany*
[b] *Karlsruhe Institute of Technology (KIT), PO Box 3640, D-76021, Karlsruhe, Germany*
[c] *Qingdao Industrial Energy Storage Research Institute, Qingdao Institute of Bioenergy and Bioprocess Technology, Chinese Academy of Sciences (QIBEBT-CAS), Qingdao, 266101, China*
[d] *Institute of Surface Chemistry and Catalysis, Ulm University, Albert-Einstein-Allee 47, D-89081, Ulm, Germany*

HIGHLIGHTS

- An 1 M $NaPF_6$-diglyme electrolyte allows stable cycling of $Na//Na_3V_2(PO_4)_2F_3$ cells.
- A polymer-inorganic cathode-electrolyte-interphase forms in this electrolyte.
- The unique surface/interfacial chemistry is comprehensively studied.
- The use of ether electrolyte enables low heat dissipation in cells.

GRAPHICAL ABSTRACT
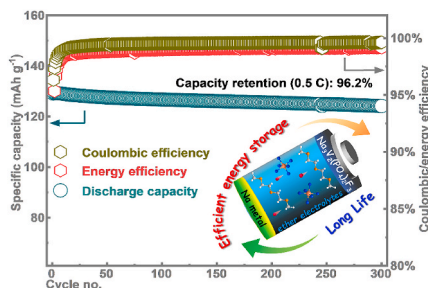
ARTICLE INFO

Keywords:
Sodium metal batteries
Cathode electrolyte interphase
Ether electrolytes
Energy efficiency
Surface chemistry

ABSTRACT

The practical utilization of ether electrolytes has long been restricted due to the concern on its electrochemical oxidation stability. Recently, it has been demonstrated that ethers are compatible with a series of polyanionic cathodes for sodium batteries. However, the specific cathode-electrolyte interface is still poorly understood. In this work, via the use of highly complementary surface and interfacial characterization techniques, we identify that the use of an 1 M $NaPF_6$-diglyme solution allows the formation of a unique polymer-inorganic cathode-electrolyte-interphase (CEI) on high-voltage $Na_3V_2(PO_4)_2F_3$ polyanionic cathodes, contributing to excellent cyclability (capacity retention of 96.2% after 300 cycles at 0.5C, 1C $\approx$ 128 mAh g^{-1}) and outstanding rate capability (124, 120 and 112 mAh g^{-1}, at 5C, 10C and 20C, respectively). The peculiar interfacial chemistry disclosed here may open up new opportunities for building high performance sodium batteries.

1. Introduction

Sodium-ion batteries (SIBs) are an emerging candidate for stationary energy storage in view of the low cost and wide abundance of sodium resources [1,2]. However, unlike the mature lithium-ion battery technology, the development of electrode and electrolyte materials for SIBs is still in its infancy. Recently, the search for suitable negative electrodes for SIBs was stimulated by the use of ether electrolytes [3]. Taking graphite as an example, its sodium storage capability can be activated in some ether electrolytes via co-intercalation chemistry, allowing for highly reversible cycling for thousands of times with a specific gravimetric capacity of ~120 mAh g^{-1} [4]. Nevertheless, this value is still far away from those obtained in LIBs (>350 mAh g^{-1}) and not relevant for practical use. Later, it was found that a certain kind of ether electrolytes (1 M NaPF$_6$ or NaBF$_4$ in ether solvents) enable the reversible cycling of tin (Sn), bismuth (Bi), hard carbon and sodium metal electrodes, respectively [5–7]. The reversible cycling of sodium metal electrodes is particularly attractive, not only because of their high theoretical capacity (1166 mAh g^{-1}) and extremely low over-potentials, but, more importantly, their wide-availability and cost-effectiveness features [7]. Starting with this sodium metal/ether electrolytes combination, it is necessary to identify a high-energy-density sodium positive electrode that is compatible with these ether electrolytes in order to maximize the energy density of sodium metal batteries.

Unfortunately, with the concern on their anodic stability, ether electrolytes have rarely been used in the tests of high-energy-density sodium positive electrodes. With an effort, Zhang et al. evaluated an ether electrolyte of 1 M NaBF$_4$-tetraglyme (TGME) for Na//P2-Na$_{2/3}$Co$_{1/3}$Mn$_{2/3}$O$_2$ cells. However, the yielded capacity retention (70%) was relatively low [8]. In comparison, ether electrolytes were found to be more compatible with polyanionic cathodes [9–11]. Among these polyanionic cathodes, NASICON-structured Na$_3$V$_2$(PO)$_2$F$_3$ has drawn the most attention in view of its high average working potential of 3.95V vs Na$^+$/Na and reasonable specific capacity (>120 mAh g^{-1}) [12]. For example, Tarascon et al. demonstrated that Na$_3$V$_2$(PO)$_2$F$_3$ electrodes could be stabilized for tens of cycles without evident capacity degradation in 1 M NaPF$_6$-diglyme (DGME) electrolyte. However, the long-term cyclic stability was not presented [13,14]. Moreover, despite the intriguing performance demonstrated, the insightful understanding of the cathode-electrolyte interfacial chemistry is still quite limited.

In this work, we systematically study the electrochemical performance of the Na$_3$V$_2$(PO)$_2$F$_3$ cathodes in a 1 M NaPF$_6$-DGME electrolyte. With a higher carbon-coating degree for Na$_3$V$_2$(PO)$_2$F$_3$ cathodes, we demonstrate that Na//Na$_3$V$_2$(PO$_4$)$_2$F$_3$ cells are capable of stable cycling for hundreds of cycles. More importantly, the surface and interfacial chemistry involved is minutely studied, concluding that the excellent electrochemical performance mostly arises from a unique polymer-inorganic cathode-electrolyte-interphase (CEI) formed.

2. Experimental section

2.1. Na$_3$V$_2$(PO$_4$)$_2$F$_3$ synthesis

A modified carbothermal solid state reaction is used for Na$_3$V$_2$(PO$_4$)$_2$F$_3$ synthesis. Briefly, 0.01 mol V$_2$O$_5$ (Pechiney), 0.02 mol NH$_4$H$_2$PO$_4$ (≥99.5%, Sigma Aldrich) and 0.025 mol carbon black (super C65, IMERYS) were first mixed in a planetary ball milling machine (ZrO2 ball to powder ratio of 20:1, Fritsch) in an air atmosphere with a rotating speed of 240 rpm for 12 h. The obtained powder was ground, pressed into pellets and subsequently annealed at 300 °C (temperature acceleration rate of 5 °C/min) for 5 h in a tube furnace in an argon flow of 0.2 L/min to evaporate possible ammonia residues. The powder product was milled again for 12 h at the same speed and a pellet was remade, which was subsequently annealed at 800 °C for 5 h to allow for carbothermal reduction and the formation of carbon-coated VPO$_4$ (c-VPO$_4$). The carbon content in the c-VPO$_4$ sample is ~10 wt% as

determined by thermogravimetric analysis in air (TGA, TGA-209F, Netzsch, Germany). Afterwards, stoichiometric amount of NaF (99.5%) was mixed with the c-VPO$_4$ sample, preliminarily ground in a mortar and afterwards ball-milled for 12 h. The resulting powder was heated for 1 h at 800 °C in argon atmosphere to allow for the formation of the final Na$_3$V$_2$(PO$_4$)$_2$F$_3$ product. The product was washed with water in a centrifuge machine and dried in a vacuum oven at 60 °C for 24 h before subsequent characterization.

2.2. Electrode preparation and cell tests

For the preparation of electrodes, active material powder, polyvinylidene fluoride (PVDF, SOLVAY SOLEF) binder and Super C65 conductive agents were mixed in a weight ratio of 80:10:10 and then dispersed in N-methyl-2-pyrrolidone (NMP), yielding a slurry with a 20 wt% solid content. This was then blade-casted on an aluminum foil with a wet thickness of 200 μm and 800 μm for normal (~2 mg cm^{-2}) and high mass loading (~7 mg cm^{-2}) electrodes. The wet electrodes were first dried at 80 °C in an oven, then punched into electrode discs (diameter: 12 mm) and finally dried in a high-vacuum Büchi oven at 100 °C. The Büchi oven vessel was sealed and taken into an ultrapure argon filled glovebox for cell assembly (MBraun LabMaster; H$_2$O content <0.1 ppm, O$_2$ content <0.1 ppm). The cells used for the electrochemical performance measurements (cycling performance, rate capability, and others) were all assembled in the 2032-type coin cells using Na$_3$V$_2$(PO$_4$)$_2$F$_3$ electrodes as working electrodes, sodium strips as counter electrodes and Whatman glass microfiber filters (GF/A) as the separator. The electrolyte amount used is 150 μL, which is excessive relative to the active materials. The cells were cycled in the voltage range between 3.0 V and 4.3 V if not otherwise specified. Cells for cyclic voltammetry measurements (CV) were assembled in Swagelok-type T-cells using Na$_3$V$_2$(PO$_4$)$_2$F$_3$ electrodes as working electrodes and sodium strips as counter and reference electrode, respectively. The CV cells were cycled between 3.0 V and 4.6 V vs Na$^+$/Na on a VMP3 multi-channel potentiostat (Bio-Logic, France) at a scan rate of 0.05 mV s^{-1}. The impedance spectra of the cycled cells were recorded on the same instrument in the frequency range between 1 MHz and 100 mHz with an amplitude potential of 5 mV. The auxiliary three-electrode cells were cycled by controlling the voltage between the working and counter electrodes in the range from 3.0 V to 4.3 V. An additional cable is used to simultaneously monitor the voltage between Na$_3$V$_2$(PO$_4$)$_2$F$_3$ working and sodium metal reference electrode. All cells tests were carried out on a battery tester (MACCOR 4300, USA) at a constant temperature of 20 ± 1 °C. The charge/discharge rate of 1C is defined as 128 mA per gram of active material in the electrode.

2.3. Characterizations

X-ray diffraction (XRD) characterization of the Na$_3$V$_2$(PO$_4$)$_2$F$_3$ powder sample and cycled electrodes was performed using a Cu-Kα source in the two-theta range from 10° to 90°, with a step size of 0.02° (Bruker D8 Advance diffractometer). The morphology of the samples was characterized using scanning electron microscopy (SEM, ZEISS 155VP Field Emission Scanning Electron Microscope operated at 5 kV). The same SEM instrument was also used to collect elemental mapping images by energy dispersive X-ray spectroscopy (EDX). Atomic force microscopy (C-AFM; Seiko, SPA-400) was employed to characterize the surface morphology of the deposits at the nanoscale. Detection of the heat flow under isothermal conditions was performed with a TAM IV microcalorimeter (TA Instruments), comprising of a custom-made sample holder for coin cells. The cells were connected with Cu-P-bronze wires (36 AWG, Lakeshore) to a VSP multi-channel potentiostat (BioLogic, France). The data presented here were acquired after internal calibration at a thermostat temperature of 20 °C. The uncertainty of the setup was less than ±300 nW. Galvanostatic cycling was conducted in the voltage-limited mode between 3.0 V and 4.3 V. A rest

step was applied after reaching the upper and lower cut-off voltage in each cycle until a heat exchange equilibrium with the environment, i.e. zero heat flow value, was reached. The heat exchanged during charge and discharge was determined by integration of the heat flow signals. Here we used a linear baseline correction in order to account for the shift during the measurement and a constant integration window of 10000s for all peaks. The recorded, total heat generation rate ($\dot{Q}_{tot}$) can be described by the simplified energy balance model developed by Newman and coworkers that proved to be valid for insertion materials [15, 16]:

$$\dot{Q}_{tot} = I\left(E_{load} \quad E_{eq}\right) + \sum_i \Delta H_i r_i + IT\left(\frac{dE_{eq}}{dT}\right) \tag{1}$$

where I is the current, E_{load} is the cell voltage under operation, E_{eq} is the equilibrium cell voltage, ΔH_i is the reaction enthalpy of a chemical side reaction i occurring at a rate r_i, T is the temperature and the quotient $\left(\frac{dE_{eq}}{dT}\right)$ is called the entropic heat coefficient, which is related to changes in the entropy by $\Delta S = nF\left(\frac{dE_{eq}}{dT}\right)$ with the proportionality constant n and Faraday's constant F.

The electrode – electrolyte interphase of cycled $Na_3V_2(PO_4)_2F_3$ electrodes was characterized by X-ray photoelectron spectroscopy (XPS). The cycled $Na_3V_2(PO_4)_2F_3$ electrodes were washed for three times with DME solvent before transferring them in a sealed, argon-filled transport vessel to the high vacuum XPS chamber, where they were inserted via a load lock system without contact to air. A monochromatic Al-K_α (hν = 1486.6 eV) X-ray source and a Phoibos 150 XPS

spectrometer were used from SPECS and Surface Concept. The data acquisition was performed at 200 W, 30 eV pass energy and 0.1 eV energy step to collect high resolution spectra. For calibration of the binding energy in the photoelectron spectra we used the C1s peak of graphitic carbon at 284.4 eV from the conductive carbon as reference. The fits were performed with the CasaXPS software, using a nonlinear Shirley-type background and a 70% Gaussian and 30% Lorentzian profile function. Time-of-flight secondary ion mass spectroscopy (TOF-SIMS) measurement (IONTOF GmbH, Münster, Germany) with Cs $^+$ sputtering was also used in the anionic mode to investigate the elemental composition of the cycled electrodes. Measurements were performed on a 150 × 150 μm^2 area. Differential elemental mass spectroscopy (DEMS) measurements were conducted in a three-electrode cell with $Na_3V_2(PO_4)_2F_3$ electrodes as positive electrodes and sodium strips as counter and reference electrode, respectively. The diameter of both electrodes is 13 mm. The cell consists of a PEEK cylinder and a PEEK U cup with a stainless steel frit, the FEP membrane coated with the cathode layer, and a gasket cut from a Teflon plate (inner diameter 7 mm, outer diameter 13 mm) positioned in between. The Measurements were performed in the potential range from 2.5 to 4.4 V *vs* Na$^+$/Na.

3. Results and discussions

3.1. Electrochemical performance of Na//Na$_3$V$_2$(PO$_4$)$_2$F$_3$ cells

The $Na_3V_2(PO_4)_2F_3$ used in this work was synthesized *via* a slightly modified carbothermal reaction (CTR) procedure introduced by Barker

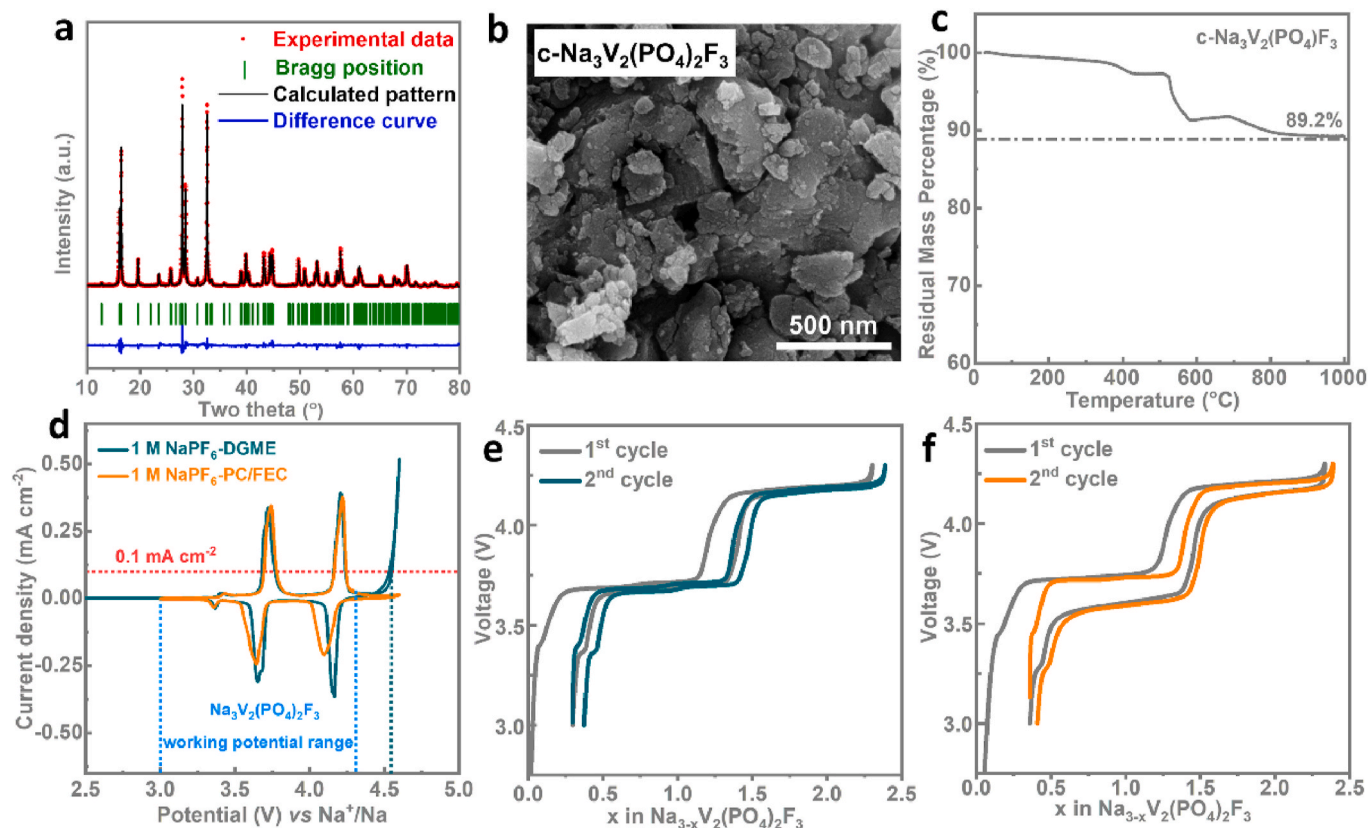**Fig. 1.** (a) Rietveld refinement of the X-ray diffraction (XRD) pattern of Na$_3$V$_2$(PO$_4$)$_2$F$_3$ sample (λ 1.54 Å). The red dots, black continuous line and bottom blue lines represent the experimentally observed, calculated and difference patterns, respectively, while the vertical green tick bars mark the reflection positions in the *Amam* space group. (b) Typical SEM image of the synthesized Na$_3$V$_2$(PO$_4$)$_2$F$_3$ powder sample. (c) TGA profile obtained via heating the Na$_3$V$_2$(PO$_4$)$_2$F$_3$ sample at a heating rate of 5 $^\circ$C min^{-1} in air. (d) Cyclic voltammetry diagrams (CV) recorded in a three-electrode cell in two kinds of electrolytes, using a Na$_3$V$_2$(PO$_4$)$_2$F$_3$ positive electrode and sodium strips as counter and reference electrodes, respectively. (e, f) Voltage profiles of Na//Na$_3$V$_2$(PO$_4$)$_2$F$_3$ cells at 0.5C obtained in 1 M NaPF$_6$-DGME electrolyte and 1 M NaPF$_6$-PC/FEC electrolyte, respectively. (For interpretation of the references to colour in this figure legend, the reader is referred to the Web version of this article.)

et al. [12] (see detailed synthesis process in the Experimental section). The X-ray diffraction pattern of $Na_3V_2(PO_4)_2F_3$ sample can be successfully refined with the Rietveld method (Fig. 1 (a) and Table S1) in the orthorhombic *Amam* space group with lattice parameters $a = 9.03911$ (44) Å, $b = 9.05273$ (39) Å, and $c = 10.76542$ (9) Å, which is in good agreement with a previous report by Croguennec et al. [12] Scanning electron microscopy (SEM) shows that the particle size is in the submicron range (0.1–1.0 µm) (Fig. 1 (b)). Elemental mapping, according to energy dispersive spectroscopy (EDS), reveals a uniform distribution of sodium, vanadium, phosphorus and carbon within the $Na_3V_2(PO_4)_2F_3$ powder sample (Fig. S1), indicating that a carbon interpenetrated $Na_3V_2(PO_4)_2F_3$ powder sample was successfully obtained. The carbon content in the powder sample is about 10.8 wt%, as determined by thermal gravimetric analysis (TGA) (Fig. 1 (c)). To gain information on the electrochemical response of the $Na_3V_2(PO_4)_2F_3$ positive electrode in different electrolytes, we performed cyclic voltammetry (CV) measurements (for experimental details see the supporting information file); the results are shown in Fig. 1 (d). Two pairs of redox peaks located at ~3.7 and 4.1 V *vs* Na^+/Na are clearly resolved both in 1 M $NaPF_6$-DGME electrolyte and a typical carbonate electrolyte (1 M $NaPF_6$ in propylene carbonate with 5 wt% fluoroethylene carbonate additive, abbreviated as 1 M $NaPF_6$-PC/FEC). These are characteristic for $Na_3V_2(PO_4)_2F_3$ electrodes and correspond to the extraction/insertion of two sodium ions

[12]. In addition to the two characteristic redox peaks for $Na_3V_2(PO_4)_2F_3$, there is no current increase up to 4.6 V *vs* Na^+/Na in the carbonate electrolyte, while it reaches 0.1 mA cm^{-2} at ~4.55 V in 1 M $NaPF_6$-DGME electrolyte. This indicates a lower anodic stability window for ether electrolytes compared with that for carbonate electrolyte, in good agreement with the result by Westman et al. [13]. However, it is noteworthy that the electrochemical stability windows of both electrolytes are well above 4.3 V vs Na^+/Na, i.e. the most often used upper cut-off voltage of $Na_3V_2(PO_4)_2F_3$ electrodes [17–21]. Therefore, both electrolytes are, in principle, fully suited for the electrochemical operation of $Na_3V_2(PO_4)_2F_3$ electrodes. Moreover, the initial charge-discharge capacity of $Na//Na_3V_2(PO_4)_2F_3$ cells is 147 mAh g^{-1} and 128 mAh g^{-1}, respectively, corresponding to an initial Coulombic efficiency of 87.1% (Fig. 1(e)), which is higher than the value of 75.4% obtained by Wang et al. in a 0.5 M $NaPF_6$-DGME electrolyte [11] and 84.7% obtained in 1 M $NaPF_6$-PC/FEC electrolyte (Fig. 1(f)).

The $Na//Na_3V_2(PO_4)_2F_3$ cell performance in different electrolytes was evaluated in 2032-type coin cells. As shown in Fig. 2 (a, b) and Fig. S2, a high capacity retention of 96.2% was obtained after 300 cycles at 0.5C (from 129 to 124 mAh g^{-1}, 1C = 128 mA g^{-1}) when using the 1 M $NaPF_6$-DGME electrolyte, much higher than that obtained in 1 M $NaPF_6$-PC/FEC electrolyte (77.5%, from 127 to 98 mAh g^{-1}). The average Coulombic efficiency (CE) of 99.5% in the ether electrolyte also
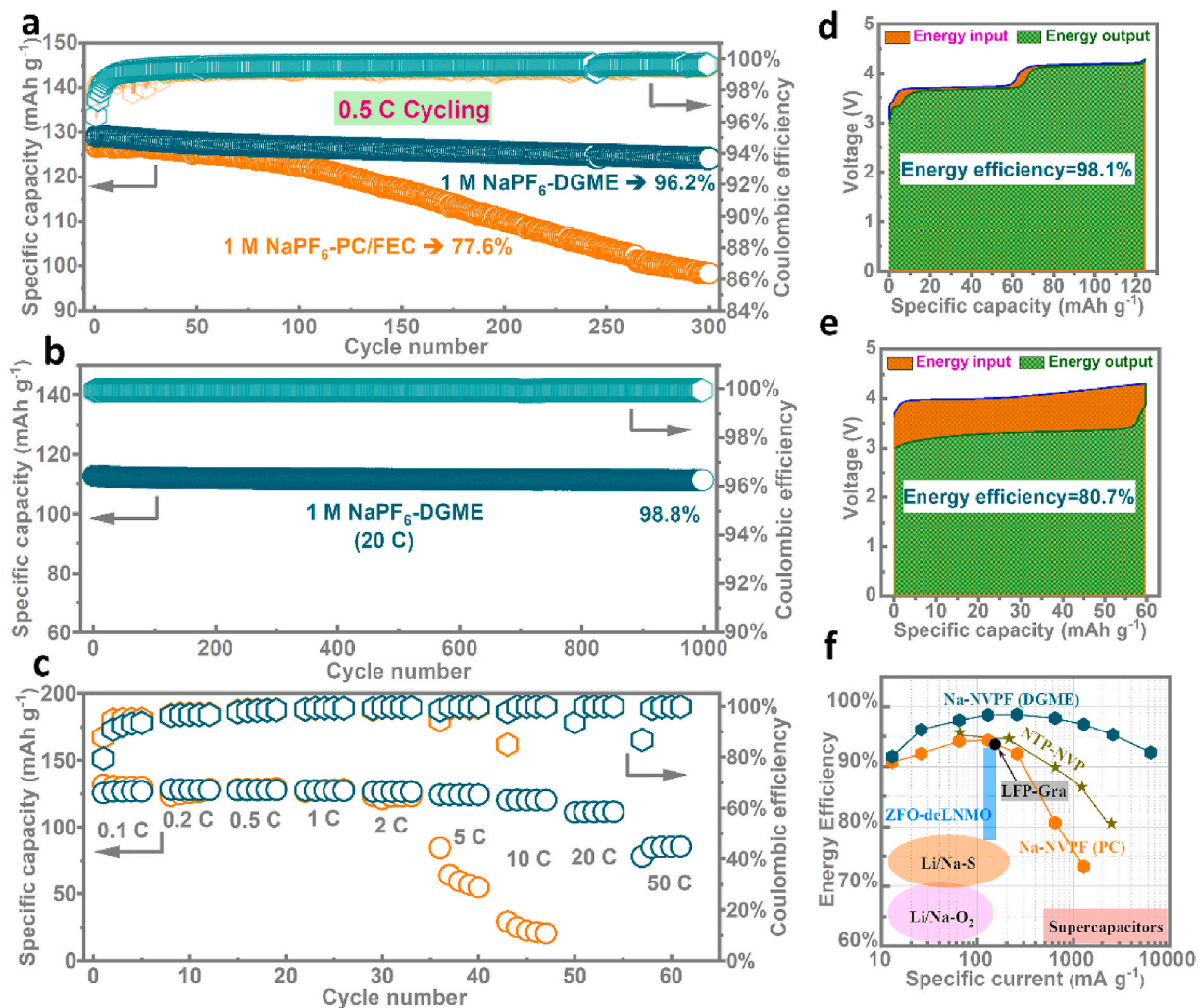

Fig. 2. (a) Comparison of the cycling stability of $Na//Na_3V_2(PO_4)_2F_3$ cells at 0.5C with different electrolytes. (b) Cycling performance of $Na//Na_3V_2(PO_4)_2F_3$ cells at 20C in 1 M $NaPF_6$-DGME electrolyte. (c) Comparison of the rate capability of $Na//Na_3V_2(PO_4)_2F_3$ cells in different electrolytes. Representative energy efficiency determination of $Na//Na_3V_2(PO_4)_2F_3$ cells at 5C in (d) 1 M $NaPF_6$-DGME and (e) 1 M $NaPF_6$-PC/FEC electrolyte via the integration of voltage-specific capacity profiles. (f) Energy efficiency comparison of various cell systems.

outperforms the 99.3% obtained in the carbonate electrolyte. More important, the excellent cycling stability could be maintained also at higher C-rates of 1C (95.0% capacity retention after 500 cycles, Fig. S3), 20C (98.8% after 1000 cycles, see Fig. 2 (b)), and even high areal loading (94.8% after 250 cycles, see Fig. S4), which is among the best for Na$_3$V$_2$(PO$_4$)$_2$F$_3$ electrodes ever reported (see detailed comparison in Table S2). Although certain improvement is still needed for commercial applications, the excellent electrochemical performance clearly demonstrates that high voltage Na$_3$V$_2$(PO$_4$)$_2$F$_3$ electrodes are well compatible with ether electrolytes, in contrast to the previous understanding that they are not suitable for high-voltage batteries [22].

In addition to the excellent cyclic stability, outstanding rate capability is also demonstrated in 1 M NaPF$_6$-DGME electrolyte. As shown in Fig. 2 (c) and Fig. S5, the cells using the ether electrolyte exhibit specific discharge capacities of 126.7, 128, 128, 127 and 127 mAh g^{-1} at 0.1C, 0.2C, 0.5C, 1C and 2C, respectively, comparable to the corresponding values of 130, 129, 129, 129 and 123 mAh g^{-1} in the carbonate electrolyte. Furthermore, at higher C-rates of 5C and 10C, the ether electrolyte still enables high specific capacities of 124 and 120 mAh g^{-1}, which by far outperform the 57 and 22 mAh g^{-1} obtained in carbonate. Even at extreme rates of 20C (~2.5 A g^{-1}) and 50C (~6 A g^{-1}), high specific capacities of 112 and 85 mAh g^{-1} can still be obtained in ether electrolyte, while the carbonate electrolyte fails to provide any capacity agreeing with most previous studies [17,19,21,23,24].

The energy efficiency (EE), i.e., the energy utilization ratio, is another key parameter for electrochemical energy storage devices. The energy efficiency is linked with the Coulombic efficiency and the voltage efficiency (i.e. EE = CE·VE, VE: average discharge voltage/average charge voltage) [25]. Benefiting from the slightly higher CE (99.5% vs

99.3%) and the substantially smaller cell voltage hysteresis (Fig. 1 (e, f)), Na//Na$_3$V$_2$(PO$_4$)$_2$F$_3$ cells display a higher EE in ether electrolytes at 0.5C than in carbonate electrolytes (99% vs 96.7%, Fig. S6). While this difference appears small, the deviation is much more significant at higher C-rates. Taking 5C (~600 mA g^{-1}) for example, the EE obtained in ether electrolyte is as high as 98.1% and far better than the 80.7% obtained for the carbonate electrolytes (Fig. 2 (d, e)). Since Na//Na$_3$V$_2$(PO$_4$)$_2$F$_3$ cells exhibit high CEs close to unity in both electrolytes, the higher EE in ether electrolytes mainly derives from the smaller cell polarization. This conclusion is supported by the much smaller Na//Na$_3$V$_2$(PO$_4$)$_2$F$_3$ cell impedance after cycling in 1 M NaPF$_6$-DGME electrolyte compared to that obtained in 1 M NaPF$_6$-PC/FEC electrolyte (Fig. S7). In fact, high EEs of over 90% can always be achieved in Na//Na$_3$V$_2$(PO$_4$)$_2$F$_3$ cells with ether electrolytes at different current rates, outperforming those of commercial Graphite//LiFePO$_4$ LIBs [26] and sodium-based cells using NASICON electrodes (e.g., NaTi$_2$(PO$_4$)$_3$//Na$_3$V$_2$(PO$_4$)$_3$ cells [27]) (Fig. 2 (f)).

3.2. Electrode surface chemistry characterization

Post-mortem analysis was conducted on the cycled electrodes to understand the distinct performance differences in the different electrolytes. Since the surface chemistry, interfacial gas evolution and ionic transport properties of sodium metal electrodes in 1 M NaPF$_6$-DGME electrolyte have been studied in detail elsewhere [7,13,28], we here mainly focus on the characterization of the positive electrode. We first performed an XRD analysis of the Na$_3$V$_2$(PO$_4$)$_2$F$_3$ electrodes, both in the pristine state and after cycling for 300 cycles. However, no change in crystal structure was observed (Fig. S8). The electrode surface
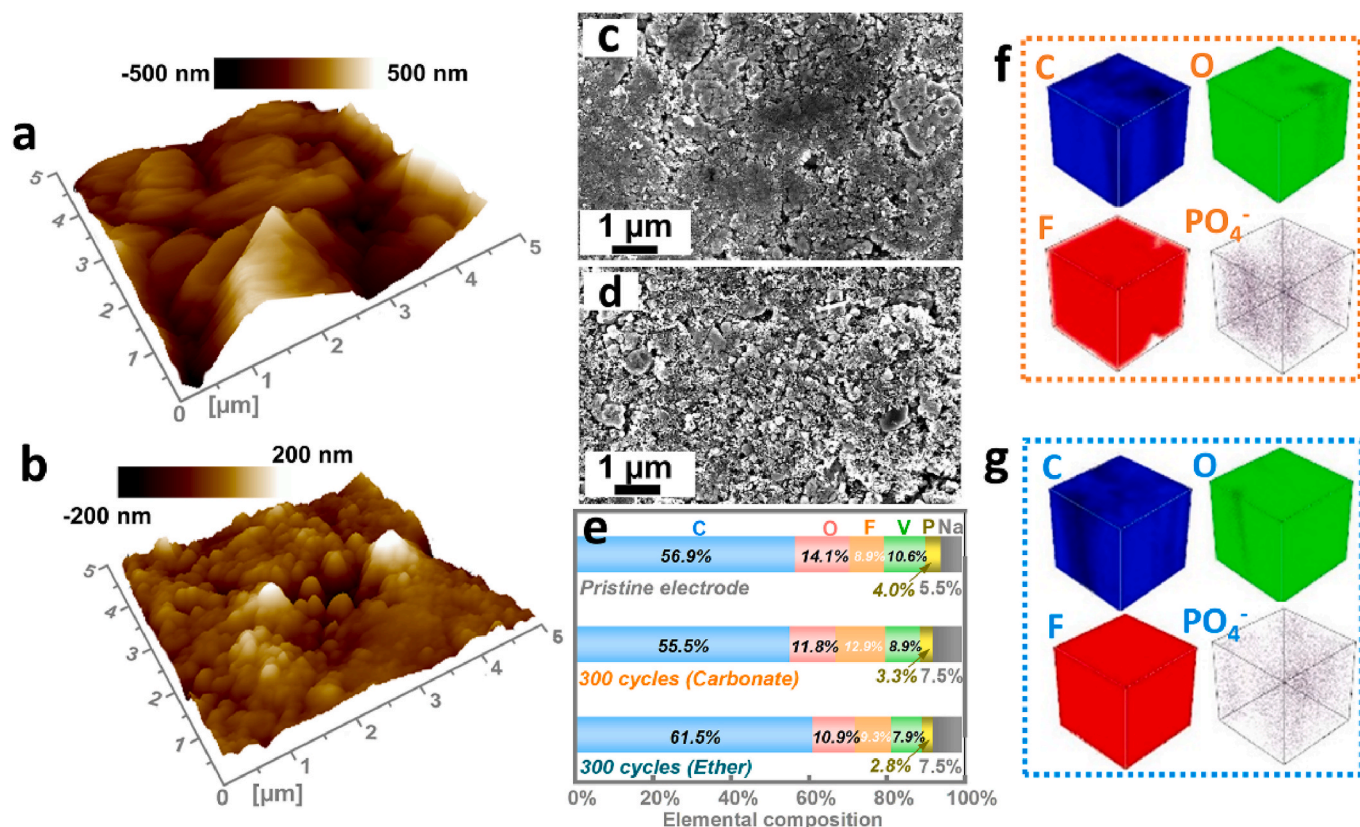

Fig. 3. Typical atomic force microscopy (AFM) images of Na$_3$V$_2$(PO$_4$)$_2$F$_3$ electrodes after 50 cycles in (a) 1 M NaPF$_6$-PC/FEC electrolyte and (b) 1 M NaPF$_6$-DGME electrolyte, respectively. Typical scanning electron microscopy (SEM) images of Na$_3$V$_2$(PO$_4$)$_2$F$_3$ morphologies after 300 cycles in (c) 1 M NaPF$_6$-PC/FEC electrolyte and (d) 1 M NaPF$_6$-DGME electrolyte, and (e) the corresponding elemental composition according to energy dispersive spectroscopy (EDS) mapping. 3-D view of C$^-$, O$^-$, F$^-$ and PO$_4^-$ species according to time-of-flight secondary-ion mass spectrometry (TOF-SIMS) analysis with sputtering from top to bottom in the selected area of Na$_3$V$_2$(PO$_4$)$_2$F$_3$ electrodes after 50 cycles in 1 M NaPF$_6$-PC/FEC electrolyte (f) and 1 M NaPF$_6$-DGME electrolyte (g), respectively.

morphology was then characterized by atomic force microscopy (AFM) and scanning electron microscopy (SEM). As shown in Fig. 3 (a, b) and (c, d), the electrodes cycled in 1 M $NaPF_6$-PC/FEC electrolyte revealed large agglomerates of particles, while individual and smaller particles are captured for those cycled in ether electrolytes. Obviously, the electrolyte has a pronounced influence on the surface evolution during cycling.

The elemental composition of the electrode surface before and after cycling was analyzed by EDS mapping; the results are illustrated in Fig. 3 (e) and Fig. S9. First, for all the electrode samples, carbon contributes most, accounting for over 50 at.%. This can be explained by the large amount of Super C65 in the electrode (10 wt%) and by carbon containing products arising from solvent decomposition. The carbon content on $Na_3V_2(PO_4)_2F_3$ electrodes cycled in 1 M $NaPF_6$-DGME electrolyte (61.5 at.%) is higher than that on the pristine electrode (56.9 at.%) and on electrodes cycled in 1 M $NaPF_6$-PC/FEC electrolyte (55.5 at.%).

Obviously, the decomposition of ether solvent results in a higher carbon content of the electrode surface layer. Second, both cycled electrodes exhibit much lower vanadium and phosphorous contents, but a higher sodium content compared with the pristine electrodes (increase from 4.0 at.% to 7.5 at.% for both electrolytes), evidencing the formation of a CEI layer covering the $Na_3V_2(PO_4)_2F_3$ particles. The formation of the CEI on the cycled electrodes is firmly supported by TOF-SIMS measurements (Fig. 3 (f, g)). They show that the surface in the sputtered range contains significant amounts of C, O and F, while there is little PO_4, which is characteristic for $Na_3V_2(PO_4)_2F_3$. Third, the amount of fluorine increases from 8.9 at.% in pristine electrodes to 12.9 at.% on the electrode cycled in 1 M $NaPF_6$-PC/FEC electrolyte, while it remains about constant (7.9 at.%) upon cycling in ether electrolytes. This underlines the pronounced contribution of FEC decomposition on the CEI formation process in 1 M $NaPF_6$-PC/FEC electrolyte.
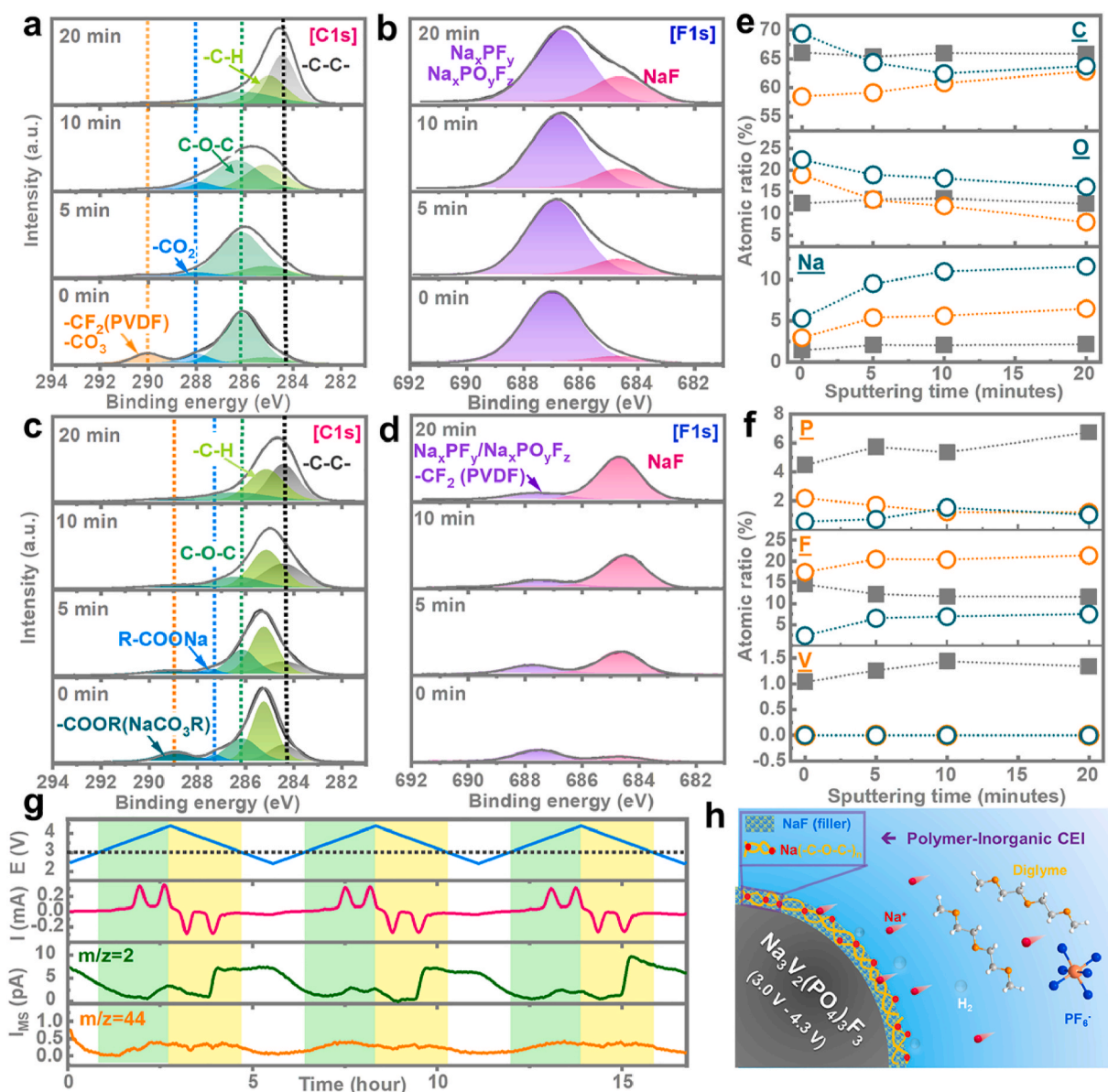
X-ray photoelectron spectroscopy (XPS) measurements, in

Fig. 4. XPS spectra of the C 1s and F 1s regions collected from the surfaces of $Na_3V_2(PO_4)_2F_3$ electrodes after 300 cycles at 0.5C in (a, b) 1 M $NaPF_6$-PC/FEC electrolyte and (c, d) 1 M $NaPF_6$-DGME electrolyte. (e, f) Variation of the elemental composition of pristine electrodes (grey) and of electrodes cycled in different electrolytes (orange for carbonate and dark blue for ether) after increasing sputter removal of the surface near region. (g) Differential electrochemical mass spectrometry (DEMS) results. (h) Schematic illustration of the SEI composition and ionic transport in ether electrolytes. (For interpretation of the references to colour in this figure legend, the reader is referred to the Web version of this article.)

combination with Ar^+ sputtering (~1 nm per minute) for depth profiling, were performed to further quantify the elemental composition and chemical species of the CEI formed on the $Na_3V_2(PO_4)_2F_3$ electrodes in the different electrolytes. Spectra obtained in the C 1s and F 1s photoemission lines after different sputtering times are shown in Fig. 4 (a–d). In the C1s region of the carbonate electrolyte case (Fig. 4 (a)), in addition to C-H and C-C species, the outermost surface layer (0 min Ar^+ sputtering) consists mainly of carbon species where carbon is bound to one (-C-O-C-, ~286.1 eV), two (–CO_2–, 288 eV) and three (–CO_3–, 290 eV) oxygen atoms, corresponding to ether, ester and carbonate species [29], respectively. These are the common species observed in the CEI formed in carbonate-based media [30–34]. Upon sputtering for 5, 10 and 20 min, the –CO_2- and –CO_3- related peaks disappear and the peak intensity of the –C-O-C related peak decreases, while peaks characteristic of -C-H / C-C- (~284.8 eV) and –C=C- (284.4 eV) species evolve. Apparently, the CEI formed in carbonate electrolyte is composed mainly of Na_2CO_3 in the outermost region, while polymeric –C-O-C- species dominate the carbon contribution in the inner part of the electrodes. Of note: Na_2CO_3 does not stabilize the positive electrode-electrolyte interface because of its high solubility [31,35–38], which may be responsible for the inferior electrochemical performance observed in 1 M $NaPF_6$-PC/FEC electrolyte. For the C1s spectra in the ether electrolyte case (Fig. 4 (b)), the outermost surface layer (0 min Ar^+ sputtering) shows –C=C- (conductive carbon, 284.4 V), -C-H/-C-C- (hydrocarbons, 284.8 eV) and -C-O-C- (ether, 286 eV) type carbon species in relatively low binding energy region. These species were also found on electrodes after cycling in carbonate electrolyte, although the contribution of the -C-H/–C-C- peak 284.4 eV is much lower here. Additionally, there are two additional peaks located at binding energies (BEs) of 287 eV and 289 eV, which are different from the carbonate electrolyte case (290 eV for –CO_3-) and we attribute to polymeric R–COONa and –COOR ($NaCO_3R$) species, respectively. Upon sputtering, the R–COONa and –COOR species related peaks disappear and the peak intensity of the –C-O-C related peak decreases, while peaks in the range of -C-H / C-C- (~284.8 eV) and –C=C- (284.4 eV) species increase in intensity. Apparently, the absence of Na_2CO_3 in the CEI in the ether electrolyte is beneficial for stabilizing the CEI thus contributing to improved cyclability.

In the F1s region, Na_xPF_y and/or $Na_xPO_yF_z$ (~687.1 eV) species, deriving from residues and/or decomposition products of the $NaPF_6$ salt, are dominant in carbonate electrolytes, accompanied by a small amount of NaF (Fig. 4 (c)). Interestingly, the contribution of NaF, resulting from the decomposition of $NaPF_6$/FEC and the dehydrofluorination of PVDF [30,32], is more pronounced in the CEI range close to the electrode (after longer sputtering time) than in the range close to the electrolyte (no sputtering). For the electrode cycled in ether electrolyte (Fig. 4 (d)), there is a significant signal of NaF already before sputtering and its relative contribution increases with increasing sputtering time. In addition, there is a small signal related to Na_xPF_y and/or $Na_xPO_yF_z$ as well as –CF_2- species related to PVDF binder. To summarize, for $Na_3V_2(PO_4)_2F_3$ electrodes cycled in ether electrolytes the CEI is mainly composed of polymeric species and inorganic NaF species (a polymer-inorganic CEI), while after cycling in carbonate electrolytes it is mainly composed of highly soluble Na_2CO_3 species and $NaPF_6$ decomposition products.

To gain a better understanding of the elemental composition of the CEI, the depth profile for the quantitative elemental analysis of the pristine electrode (its detailed chemical information is not provided in this manuscript, and will be characterized in our future work) and cycled electrodes after different sputtering times were plotted and compared in Fig. 4 (e, f). Overall, the elements that originate from $Na_3V_2(PO_4)_2F_3$, for example V and P, are present in a sizable amount at any sputtering depth of the pristine electrodes, while their amounts are negligible on cycled $Na_3V_2(PO_4)_2F_3$ electrodes. This results from and undoubtedly demonstrate again the formation of a CEI layer on the cycled electrodes, covering the original $Na_3V_2(PO_4)_2F_3$ electrodes. As

for the two cycled electrodes, we find more C, O and Na, but less F on the $Na_3V_2(PO_4)_2F_3$ electrodes cycled in ether electrolyte than that cycled in carbonate-based electrolyte. This is in agreement with the EDS mapping results, further demonstrating that the CEI formed in ether electrolytes is mainly composed of ether solvent decomposition products, while the CEI formed on the electrodes cycled in carbonate-based electrolytes exhibit a larger amount of F, highlighting again the important contribution of FEC decomposition.

3.3. Cathode-electrolyte interfacial gassing analysis

DEMS measurements were performed to identify the gaseous products evolving at the interface between $Na_3V_2(PO_4)_2F_3$ and ether electrolyte, with the aim to understand the CEI formation process during cell operation; the results are shown in Fig. 4 (g). In the selected ion current signals monitored, only the signals at $m/z = 2$ and $m/z = 44$ show a repetitive potential dependence, while the other mass signals are rather featureless (e.g., $m/z = 28$; see the mass signals representative for other gases in Fig. S10). Quantitatively, the ion current intensity of $m/z = 44$ is much smaller than that of H_2 and always maximizes at relatively high potentials, presumably related to the mild oxidative decomposition of the ether solvents (see also Figs. S10 and S11). As for the $m/z = 2$ signal, i.e., H_2 gas, its evolution is highly periodic, however, rather complex. High H_2 evolution rates are obtained close to the open-circuit potential (ca. 2.3 V vs. Na^+/Na). Upon charging, the H_2 formation rate first gradually decays up to ca. 3.5 V (vs. Na^+/Na). Upon further increase in potential, the H_2 formation rate increases only slightly, reaching a local maximum, which corresponds to the pronounced current peaks for vanadium oxidation and de-sodiation. Upon discharge, the H_2 ion current decreases to a minimum value close to zero, and then steeply increases when passing the second vanadium reduction peak to complete re-sodiation. Here it reaches a broad high ion current plateau of ~8 pA, which extends until the lower cut-off potential of 2.3 V. According to a work by Gasteiger et al., the generation of H_2 is largely related to the reduction of protic electrolyte oxidation species (R-H^+) formed at the positive electrode. Moreover, the higher is the upper cut-off voltage, the more R-H^+ and H_2 is generated [39]. This argument is firmly supported by potential-step DEMS measurements (Fig. S11), showing that (i) a higher H_2 generation plateau is observed when a 4.5 V potential step is applied compared to that of 4.0 V (ii) the $m/z = 2$ ion current did not decay when returning to the open circuit potential (OCP), but rather increased, indicating the H_2 generation mostly derives from the reduction of species in the electrolyte. Of note, in our specific case here, the H_2 generation plateau starts from a relatively high potential of ~3.6 V *vs* Na^+/Na, corresponding to the insertion of the second sodium ion, which is most likely due to the catalytic effect of $Na_{2+x}V_2(PO_4)_2F_3$. Although it is still challenging to decipher the detailed electrochemical processes behind the periodic evolution of H_2, it is not related to H_2O reduction generated at the sodium counter electrode, which is generally considered as an irreversible process and present mainly in the initial cycle. H_2 evolution at the negative electrode can also be ruled out as origin of the H_2 ion current signal in view of our specific DEMS cell configuration [40]. Considering that the ether solvent is the only available species containing hydrogen, and the fact that polymeric species are evidenced in the CEI (Fig. 4(b), (d)), the dehydrogenation process is most probably related to polymerization/oligomerization reactions of ether [40]. Moreover, such CEI species, mainly composed of a polymer matrix filled with inorganic NaF particles (see the schematic illustration in Fig. 4 (h)) could be highly impermeable for electrolytes, thus alleviating side reactions at the positive electrode-electrolyte interface, which supports the ultrastable cycling of $Na_3V_2(PO_4)_2F_3$ electrodes (Fig. 2 (a, b)). Also, the CEI must be highly ion conductive to facilitate rapid ionic transport at the positive electrode-electrolyte interface, as indicated by the excellent rate capability of $Na//Na_3V_2(PO_4)_2F_3$ cells in ether electrolytes and their extremely small impedance after 300 cycles (Fig. S7).

3.4. Heat generation in Na//Na₃V₂(PO₄)₂F₃ sodium metal cells

Operando isothermal microcalorimetry (*operando* IMC) has been demonstrated to be an effective tool in determining the heat generated and for deconvolution of the different contributions to the heat flow [40–44]. It is used here to differentiate the heat generation, especially the heat dissipation (i.e., polarization heat + parasitic heat), during Na//Na₃V₂(PO₄)₂F₃ cell operation in different electrolytes with an aim to understand their interfacial compatibility (Fig. 5 (a)). Positive values of the heat generation rate indicate heat flow that is released by the cell and negative values indicate that taken up by the cell. The measured heat generation rate is considered to be constituted by three different sources [45,46]:

$$\dot{Q}_{tot} = \dot{Q}_{polarization} + \dot{Q}_{parasitic} + \dot{Q}_{rev} \tag{2}$$

where $\dot{Q}_{polarization}$ is the irreversible heat flow originating from ohmic losses, charge transfer as well as mass transfer limitations, $\dot{Q}_{parasitic}$ the heat flow generated by secondary reactions and $\dot{Q}_{rev}$ being the reversible heat flow originating from changes in entropy. The total heat exchanged with the environment per half cycle was determined by integration of the heat generation rate (Fig. 5 (b, c)).

Starting from the 2nd cycle, the heat generation rate profiles of the charge and discharge steps became reproducible. Here, we used the 5th cycle, where the heat generation has completely stabilized, for quantitative analysis (Fig. 5 (d, e)). Specifically, during discharge, the heat generation rate in the ether electrolyte-containing cell is only about one fourth of that in the carbonate electrolyte containing cell (Fig. 5 (e)). More notably, it even bore a negative sign **during charge** in ether electrolyte implying absorption of heat by the cell during sodium extraction from Na₃V₂(PO₄)₂F₃. The take-up of heat must be caused by changes in entropy during de-sodiation, since the first two terms of the energy balance model (equation (1)) will by definition always result in positive values. Therefore, it is concluded that $\dot{Q}_{rev}$ provides the dominant contribution to $\dot{Q}_{tot}$ while the heat dissipation, in the form of $\dot{Q}_{polarization}$ and $\dot{Q}_{parasitic}$, is rather small in the ether electrolyte-containing cell, corresponding to the high energy efficiencies (Fig. 2 (d, f)). Since the same faradaic reaction occurs independently from the electrolyte used, the same or at least comparable course of the entropic heat flow rate is expected in different electrolytes. In fact, the heat flow rate profiles of ether and carbonate electrolyte-containing cell match quite well, except an additional feature at approx. 0.075 mAh in the former case (labelled with "◇" in Fig. 5 (d)). Yet, the nature of this feature is unknown at present. More importantly, we could indeed well "simulate" the heat flow signal of the sample with carbonate electrolyte by simply adding a constant value to the heat flow of the DGME electrolyte cell (see the dotted line in Fig. 5 (d, e)). This illustrates that there is an additional heat flow source that provides a nearly constant contribution to $\dot{Q}_{tot}$ in the carbonate electrolyte containing cell over the whole SOC range, which is correlated with the lower energy efficiency (Fig. S6, Fig. 2 (e, f)). Since parasitic reactions are typically voltage dependent, cells with carbonate electrolytes must exhibit a larger cell polarization, responsible for constant surplus heat generation. Interestingly, the
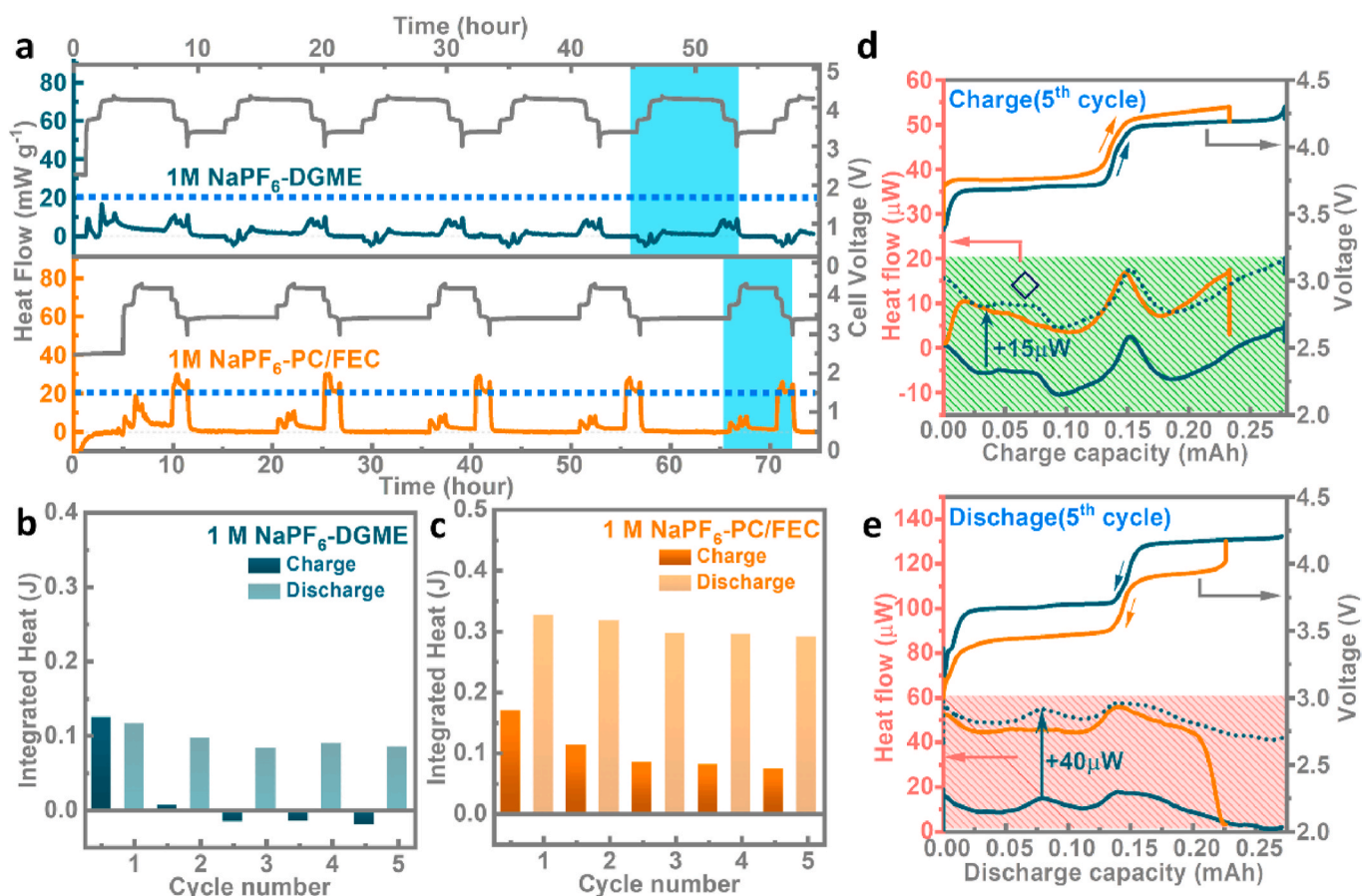

Fig. 5. (a) Overall heat flow and charge-discharge profiles obtained by *operando* IMC measurements for Na//Na₃V₂(PO₄)₂F₃ cells with different electrolytes. The heat generation rate was integrated for each half cycle in (b) 1 M NaPF₆-DGME electrolyte and (c) 1 M NaPF₆-PC/FEC electrolyte, respectively. Combined plots of the heat flow and the respective voltage curve of Na//Na₃V₂(PO₄)₂F₃ cells during (d) charge and (e) discharge process in the 5th cycle. (Cyan lines represent ether electrolytes and orange lines carbonate electrolytes while the dotted lines are the simulated heat flow by simply adding a constant value to the heat flow of the DGME electrolyte cell). (For interpretation of the references to colour in this figure legend, the reader is referred to the Web version of this article.)

polarization is less during charge and larger during discharge. This could be partly explained by the polarization of sodium metal electrodes in carbonate electrolytes, showing smaller and larger over-potentials in the charge and discharge processes, respectively. In contrast, in ether electrolyte the over-potentials of sodium metal electrodes are negligible (Fig. S12). In summary, IMC results show that utilization of ether electrolytes tremendously lowers the heat generation and dissipation for $Na//Na_3V_2(PO_4)_2F_3$ cells compared to the commonly used carbonate-based electrolytes, indicating minimized interfacial parasitic reactions and fast charge-transfer kinetics, which is highly promising for building safe and energy-efficient batteries.

4. Conclusion

We performed a comprehensive study on the use of ether electrolytes for high-voltage $Na_3V_2(PO_4)_2F_3$ electrodes. It is demonstrated that the use of this specific ether electrolyte (1 M $NaPF_6$-Diglyme) allows the formation of an effective polymer-inorganic CEI on the $Na_3V_2(PO_4)_2F_3$ electrodes, enabling stable cycling and fast charge-transfer for $Na_3V_2(PO_4)_2F_3$ cathodes. Overall, the paramount performance of $Na_3V_2(PO_4)_2F_3$ electrodes achieved is in contrast to previous understanding that ether electrolytes are not suitable for high voltage batteries.

CRediT authorship contribution statement

Bingsheng Qin: synthesized the positive electrode material, performed SEM, XRD, TGA and electrochemical measurements and, Writing – original draft, the manuscript. **Maider Zarrabeitia:** respectively, conducted the XPS and IMC measurements and, Formal analysis, the results. **Alexander Hoefling:** respectively, conducted the XPS and IMC measurements and, Formal analysis, the results. **Zenonas Jusys:** contributed to the DEMS characterizations. **Xu Liu:** performed the refinement of the XRD results, and contributes to the writing and organization of the manuscript. **R. Jurgen Behm:** contributed to the DEMS characterizations. **Guanglei Cui:** provided funding for the work. **Alberto Varzi:** Supervision, the experimental and writing work. **Stefano Passerini:** provided funding for the work, coordinated all the activities for this work, All authors revised the manuscript.

Declaration of competing interest

The authors declare that they have no known competing financial interests or personal relationships that could have appeared to influence the work reported in this paper.

Data availability

The data that has been used is confidential.

References

[1] N. Yabuuchi, K. Kubota, M. Dahbi, S. Komaba, Chem. Rev. 114 (2014) 11636–11682.
[2] C. Vaalma, D. Buchholz, M. Weil, S. Passerini, Nat. Rev. Mater. 3 (2018), 18013.
[3] J. Zhang, D.-W. Wang, W. Lv, L. Qin, S. Niu, S. Zhang, T. Cao, F. Kang, Q.-H. Yang, Adv. Energy Mater. 8 (2018), 1801361.
[4] B. Jache, P. Adelhelm, Angew. Chem., Int. Ed. Engl. 53 (2014) 10169–10173.
[5] B. Zhang, G. Rousse, D. Foix, R. Dugas, D.A.D. Corte, J.-M. Tarascon, Adv. Mater. 28 (2016) 9824–9830.
[6] C. Wang, L. Wang, F. Li, F. Cheng, J. Chen, Adv. Mater. 29 (2017) 1702212.
[7] Z.W. Seh, J. Sun, Y. Sun, Y. Cui, ACS Cent. Sci. 1 (2015) 449–455.
[8] P.M.L. Le, T.D. Vo, H. Pan, Y. Jin, Y. He, X. Cao, H.V. Nguyen, M.H. Engelhard, C. Wang, J. Xiao, J.-G. Zhang, Adv. Funct. Mater. 30 (2020), 2001151.
[9] M.K. Sadan, H. Kim, C. Kim, S.H. Cha, K.-K. Cho, K.-W. Kim, J.-H. Ahn, H.-J. Ahn, J. Mater. Chem. 8 (2020) 9843–9849.
[10] H.-J. Liang, Z.-Y. Gu, X.-X. Zhao, J.-Z. Guo, J.-L. Yang, W.-H. Li, B. Li, Z.-M. Liu, W.-L. Li, X.-L. Wu, Angew. Chem., Int. Ed. Engl. 60 (2021) 26837–26846.
[11] Y.-Q. Zheng, M.-Y. Sun, F.-D. Yu, L. Deng, Y. Xia, Y.-S. Jiang, L.-F. Que, L. Zhao, Z.-B. Wang, Nano Energy 102 (2022), 107693.
[12] M. Bianchini, N. Brisset, F. Fauth, F. Weill, E. Elkaim, E. Suard, C. Masquelier, L. Croguennec, Chem. Mater. 26 (2014) 4238–4247.
[13] K. Westman, R. Dugas, P. Jankowski, W. Wieczorek, G. Gachot, M. Morcrette, E. Irisarri, A. Ponrouch, M.R. Palacín, J.M. Tarascon, P. Johansson, ACS Appl. Energy Mater. 1 (2018) 2671–2680.
[14] C. Cometto, G. Yan, S. Mariyappan, J.-M. Tarascon, J. Electrochem. Soc. 166 (2019) A3723–A3730.
[15] D. Bernardi, A general energy balance for battery systems, J. Electrochem. Soc. 132 (1985) 5.
[16] L.E. Downie, J.R. Dahn, Determination of the voltage dependence of parasitic heat flow in lithium ion cells using isothermal microcalorimetry, J. Electrochem. Soc. 161 (2014) A1782–A1787.
[17] S. Liu, L. Wang, J. Liu, M. Zhou, Q. Nian, Y. Feng, Z. Tao, L. Shao, J. Mater. Chem. 7 (2019) 248–256.
[18] L. Deng, G. Sun, K. Goh, L.-L. Zheng, F.-D. Yu, X.-L. Sui, L. Zhao, Z.-B. Wang, Electrochim. Acta 298 (2019) 459–467.
[19] J. Zhao, Y. Gao, Q. Liu, X. Meng, N. Chen, C. Wang, F. Du, G. Chen, Chem. Eur J. 24 (2018) 2913–2919.
[20] H. Xiong, Y. Liu, Y. Yang, H. Shao, J. Electrochem. Soc. 165 (2018) A746–A756.
[21] C. Zhu, C. Wu, C.-C. Chen, P. Kopold, P.A. van Aken, J. Maier, Y. Yu, Chem. Mater. 29 (2017) 5207–5215.
[22] P.K. Nayak, L. Yang, W. Brehm, P. Adelhelm, Angew. Chem., Int. Ed. Engl. 57 (2018) 102–120.
[23] Y. Cai, X. Cao, Z. Luo, G. Fang, F. Liu, J. Zhou, A. Pan, S. Liang, Adv. Sci. 5 (2018), 1800680.
[24] C. Shen, H. Long, G. Wang, W. Lu, L. Shao, K. Xie, J. Mater. Chem. 6 (2018) 6007–6014.
[25] J. Asenbauer, A. Varzi, S. Passerini, D. Bresser, J. Power Sources 473 (2020), 228583.
[26] P. Meister, H. Jia, J. Li, R. Kloepsch, M. Winter, T. Placke, Chem. Mater. 28 (2016) 7203–7217.
[27] H. Zhang, B. Qin, D. Buchholz, S. Passerini, ACS Appl. Energy Mater. 1 (2018) 6425–6432.
[28] L. Lutz, D. Alves Dalla Corte, M. Tang, E. Salager, M. Deschamps, A. Grimaud, L. Johnson, P.G. Bruce, J.-M. Tarascon, Chem. Mater. 29 (2017) 6066–6075.
[29] R.I.R. Blyth, H. Buqa, F.P. Netzer, M.G. Ramsey, J.O. Besenhard, P. Golob, M. Winter, Appl. Surf. Sci. 167 (2000) 99–106.
[30] M.A. Muñoz-Márquez, M. Zarrabeitia, E. Castillo-Martínez, A. Eguía-Barrio, T. Rojo, M. Casas-Cabanas, ACS Appl. Mater. Interfaces 7 (2015) 7801–7808.
[31] M. Zarrabeitia, L. Gomes Chagas, M. Kuenzel, E. Gonzalo, T. Rojo, S. Passerini, M. ´ Muñoz-Márquez, ACS Appl. Mater. Interfaces 11 (2019) 28885–28893.
[32] M. Dahbi, T. Nakano, N. Yabuuchi, S. Fujimura, K. Chihara, K. Kubota, J.-Y. Son, Y.-T. Cui, H. Oji, S. Komaba, Chemelectrochem 3 (2016) 1856–1867.
[33] M. Galceran, J. Rikarte, M. Zarrabeitia, M.C. Pujol, M. Aguiló, M. Casas-Cabanas, ACS Appl. Energy Mater. 2 (2019) 1923–1931.
[34] S. Doubaji, B. Philippe, I. Saadoune, M. Gorgoi, T. Gustafsson, A. Solhy, M. Valvo, H. Rensmo, K. Edström, ChemSusChem 9 (2016) 97–108.
[35] A. Ponrouch, D. Monti, A. Boschin, B. Steen, P. Johansson, M.R. Palacín, J. Mater. Chem. 3 (2015) 22–42.
[36] D.I. Iermakova, R. Dugas, M.R. Palacín, A. Ponrouch, J. Electrochem. Soc. 162 (2015) A7060–A7066.
[37] R. Mogensen, D. Brandell, R. Younesi, ACS Energy Lett. 1 (2016) 1173–1178.
[38] G.G. Eshetu, S. Grugeon, H. Kim, S. Jeong, L. Wu, G. Gachot, S. Laruelle, M. Armand, S. Passerini, ChemSusChem 9 (2016) 462–471.
[39] M. Metzger, B. Strehle, S. Solchenbach, H.A. Gasteiger, J. Electrochem. Soc. 163 (2016) A798–A809.
[40] B. Qin, A. Schiele, Z. Jusys, A. Mariani, T. Diemant, X. Liu, T. Brezesinski, R. J. Behm, A. Varzi, S. Passerini, ACS Appl. Mater. Interfaces 12 (2020) 3697–3708.
[41] D. Tewari, P.P. Mukherjee, J. Mater. Chem. 7 (2019) 4668–4688.
[42] M.M. Huie, D.C. Bock, L. Wang, A.C. Marschilok, K.J. Takeuchi, E.S. Takeuchi, J. Phys. Chem. C 122 (2018) 10316–10326.
[43] G. Assat, S.L. Glazier, C. Delacourt, J.-M. Tarascon, Nat. Energy 4 (2019) 647–656.
[44] B. Qin, T. Diemant, H. Zhang, A. Hoefling, R.J. Behm, J. Tübke, A. Varzi, S. Passerini, ChemSusChem 12 (2019) 2609–2619.
[45] D. Bernardi, J. Electrochem. Soc. 132 (1985) 5.
[46] L.E. Downie, J.R. Dahn, J. Electrochem. Soc. 161 (2014) A1782–A1787.